Dynamic B_0 Shimming for Multi-band Imaging using High Order Spherical Harmonic Shims

[1]HP Hetherington, [1]CH Moon, [2]M Schwerter, [2,3,4,5]J Shah and [1]JW Pan

[1]Department of Radiology, University of Pittsburgh, Pittsburgh USA.

[2]Institute of Neuroscience and Medicine 4, INM-4, Forschungszentrum Jülich, Germany.

[3]Institute of Neuroscience and Medicine 11, INM-11, JARA, Forschungszentrum Jülich, Germany.

[4]JARA - BRAIN - Translational Medicine, Aachen, Germany.

[5]Department of Neurology, RWTH Aachen University, Aachen, Germany.

Words: 4992

Figures: 7

Tables: 3

References: 35

Running title: Dynamic multi-band B_0 shimming

Keywords: multi-band shimming, spherical harmonics, constrained optimization, echo planar imaging, image distortion

Funding provided by: National Institutes of Health R01s EB024408, NS081772, NS090417

Corresponding Author:
Hoby Hetherington
Department of Radiology
University of Pittsburgh
Pittsburgh PA, 15213

Abstract

Purpose: To describe and implement a strategy for dynamic slice-by-slice and multi-band B_0 shimming using spherical harmonic shims in the human brain at 7T.

Theory: For thin axial slices, spherical harmonic shims can be divided into pairs of shims (z-degenerate and non-z-degenerate) which are spatially degenerate, such that only ½ of the shims (non-z-degenerate) are required for single slice optimizations. However, when combined, the pairs of shims can be used to simultaneously generate the same in-plane symmetries but with different amplitudes as a function of their z location. This enables multi-band shimming equivalent to that achievable by single slice-by-slice optimization.

Methods: All data were acquired at 7T using a spherical harmonic shim insert enabling shimming up through 4th order with two additional 5th order shims (1st-4^{th+}). Dynamic shim updating was achieved using a 10A shim power supply with 2ms ramps and constrained optimizations to minimize eddy currents.

Results: In groups of 8 subjects we demonstrated that: 1) dynamic updating using 1st-4^{th+} order shims reduced the standard deviation of the B_0 field over the whole brain from 32.4±2.6 and 24.9±2Hz with 1st-2nd and 1st-4^{th+} static global shimming to 15.1+1.7Hz; 2) near equivalent performance was achieved when dynamically updating only the non-z-degenerate shims (14.3+1.5Hz), or when a using multi-band shim factor of 2, MB_s=2, and all shims (14.4+2.0Hz).

Conclusion: High order spherical harmonics provide substantial improvements over static global shimming and enable dynamic multi-band shimming with near equivalent performance to that of dynamic slice-by-slice shimming. This reduces distortion in echo-planar imaging.

Introduction

The importance of B_0 shimming and its impact on image distortion for echo planar imaging has been recognized for many years [1-3]. Technological development to improve B_0 homogeneity through higher spatial order geometrical corrections has included the use of passive shims [4, 5], high order spherical harmonic (SH) shims [6-8], multi coil (MC) arrays [9-13] and methods to maximize the effectiveness of the available hardware through dynamic updating [14-18]. For the human brain, optimizing the B_0 shim corrections on a slice-by-slice (SBS) basis using dynamic shim updating (DSU) as opposed to a single global solution over the majority or the entire brain, can significantly improve homogeneity. Because of this, several groups have developed DSU approaches, including strategies for optimization and pre-emphasis mitigation [19-22].

One of the key observations in SBS high order spherical harmonic shimming of axial slices is that the solution space is relatively soft, i.e., constrained optimization of the shim current can be readily applied with minimal impact on the achieved homogeneity [20, 23]. These observations are due in part to the use of thin axial slices and the spatial degeneracy of spherical harmonics when variation in B_0 field along the z-direction is minimal. This enables multi-band shimming (MB_s), i.e., simultaneously shimming multiple spatially separate slices[24] or slabs [25] as described for multi-coil arrays. This construct is particularly relevant given the importance of multi-band imaging for diffusion tensor imaging and fMRI.

In this paper, we examine and demonstrate the performance of a very high order shim (VHOS) insert based on spherical harmonic geometries to achieve dynamic SBS and MB_s. Starting with a dynamic (MB_s=1, i.e. SBS) acquisition, we describe the spatial symmetries required for MB_s. We demonstrate the shimming improvement with DSU for SBS and MB_s=2 in n=8 healthy subjects. We also demonstrate the reduction in spatial distortion in MB=2 spin echo EPI. Finally, we discuss the potential improvements for higher MB factor dynamic shimming (MB_s=3 or 4) with the existing spherical harmonic shim insert.

Theory

Spherical Harmonics, z-degeneracy, DSU and multi-band shimming

Although SH shims form an orthogonal basis set, the individual shims fields can become spatially degenerate under certain conditions [26]. For thin axial slices, SH shims that only differ by a multiplicative factor in z will have effectively identical in-plane spatial dependencies (Figure 1). For purposes of visualization, each image (other than **Z0** and **Z**) is scaled to use the full color range.

Therefore, it is useful to consider the dependence of the B_0 field generated by the SHs as a function of z. Table 1 divides these functions (up to 4th order) into terms that differ by only a linear z-dependence and constant offset, here denoted as non-z-degenerate, NzD, and z-degenerate, zD. The NzD fields provide in-plane complexity, while the zD fields replicate the same in-plane symmetry of the NzD shims but carry an additional linear z-dependence (i.e. those with no amplitude when the slice offset=0, Fig. 1). Based on this partitioning, half of the available harmonics are z-degenerate for thin axial slices. Since the zD shims are redundant for thin axial target slices, the optimal correction field can be generated from a reduced set of functions as given by Eq. 1. [16],

$$B_0(x,y,z) = a_0\mathbf{Z0} + \sum_{i=1}^{n} a_i \boldsymbol{A}_i^{NzD}(x,y) \qquad [1]$$

where a_0 and a_i are scaling coefficients, there are n shims and $\boldsymbol{A}_i^{NzD}$ reflects the in-plane spatial dependence of the i^{th} NzD shim. In this discussion, spatial coordinates are referred to by lower case letters (e.g. x, y, z), while SH symmetries (e.g. **Z0**) are referred to by bold upper-case characters. Conversely, this implies that an identical shim field can be generated using the zD shims only, for which the zD_i terms are scaled by their position along the z-axis and a scaling coefficient relative to their non-degenerate partners, NzD_i, where b_0 and b_1 are scaling coefficients and $\boldsymbol{A}_i^{zD}(x,y)$ is the in-plane spatial dependence of the ith zD shim and z is the spatial offset along the z axis.

$$\boldsymbol{A}_i^{zD}(x,y) = b_0*\mathbf{Z0} + b_1*z * \boldsymbol{A}_i^{NzD}(x,y) \qquad [2]$$

This assumes that all individual terms with a z^n spatial dependence can be approximated to be a constant value across the thin slice. For example, with an arbitrarily thin axial slice at position z, the effect of the NzD shim **X** can be replicated by its zD partner shim, **ZX,** through use of a scaling factor b_1*z (see Table 1). As a result, a linear combination of **X** and **ZX** (NzD and zD respectively) shims can simultaneously generate two different in plane pure **X** fields at two unique z positions. This assumes that the two slices are sufficiently separated spatially and that the available strength of the zD shims can generate the needed differences in B_0 field. As shown in Table 1, with all harmonics classified as zD or NzD, this simple logic applies to all shims on the current shim insert with the exception of the "unpaired NzD" terms **Z2C2** and **Z2S2**. If these unpaired terms have minimal impact on the overall single slice in-plane homogeneity, this effectively enables multiband shimming (MB_s=2) of thin axial slices with nearly equivalent performance as DSU-SBS. However, it should be noted that imperfections in the SHs, i.e. both

higher and lower order/degree symmetries can alter the achieved results for MB_s=2 depending upon slice position and individual anatomy.

Methods

General Hardware Configuration

All data were acquired at 7T on a Siemens whole body system equipped with 8 channels for parallel transmission and a 16-channel transceiver array [27, 28]. The transceiver array consists of 2 rows in the z direction, 8 coils per row and is driven by 8 independent transmit channels feeding 8 1->2 power splitters. The output from each power splitter is routed to coils at the same azimuthal position across the two rows. B_1 shimming was performed to optimize B_1 homogeneity [28, 29].

For consistency with the majority of previous work in the MR literature, spherical harmonic (SH) terms are described by their order and degree, with the degree describing the x-y plane periodicity. A VHOS 38cm inner diameter 18 channel shim insert, Resonance Research Inc. (RRI) Billerica MA., was used, that incorporates **Z0**, all seven 3rd order shims, eight 4th order shims (excluding **Z4**) and two 5th order shims (**ZC4**, **ZS4**), altogether denoted as 1st-4th+ shims. Second order shims were provided by the shims resident on the gradient coil. The **Z0,** 2nd, 3rd and 4th+ order shims, were driven by a 10 A/channel RRI shim power supply equipped with a dynamic shim updating (DSU) unit providing 1024 time points per channel with pre-emphasis. The linear offsets were updated within the modified acquisition sequence using a text file as input. Pre-emphasis (15% maximum) was only needed for **Z0** and the 2nd order shims resident on the gradient set [20]. The RRI power supply values and the pulse sequence were synchronized by use of an external trigger pulse from the scanner console to the RRI power supply clocked 2ms prior to the RF excitation pulse.

General B_0 Mapping Parameters and Optimization

All B_0 maps were acquired with 5 evolution times (ΔTE=1,2,4,8ms) [30] using contiguous 3mm slices with 64x64 in-plane resolution. The field of view, FOV, and numbers of slices were varied according to the experimental objectives and detailed below. To optimize the B_0 field homogeneity, a least squares optimization (using the MATLAB *fmincon* function) was performed using constraints on the maximum current for each individual channel (5A, i.e. ½ of the maximum current available) and a constraint on the maximum aggregate current (see below). The aggregate current is defined as the sum

of the absolute value of the current applied to all channels. The spatial distribution of the B_0 field generated by each shim was measured experimentally and modeled using a basis set of 10^{th} order spherical harmonics to account for deviations in the generated fields from their theoretical representations. As such, the modeled shim fields are not completely orthogonal, but the imperfections are included in the optimization process. For the purposes of comparison to other shim hardware, Table 1 lists the strength of the primary component of each shim channel in Hz/mm^n at a current of 5A.

Constrained Optimization

To minimize the potential for inducing eddy currents during the fast switching of shim currents and errors associated with small inaccuracies in shim strength, we evaluated the impact of using a constraint on the maximum aggregate shim current. To empirically determine a suitable maximum aggregate current constraint, B_0 maps were acquired from 10 subjects using 41 contiguous 3-mm thick slices, 64x64 image matrix size over a FOV of $240x240mm^2$. The predicted residual B_0 inhomogeneity using 1^{st}-4^{th+} order shimming was then calculated as a function of a maximum aggregate current boundary condition with the maximum aggregate current constraint varying in 5A increments from 5 to 50A. An unconstrained solution was also calculated for reference purposes. Four representative brain regions (3 adjacent slices forming each ROI) containing the cerebellum (CBL), medial temporal lobe (MTL), subcortical nuclei (SCN) and the supplementary motor area (SMA) were selected for analysis.

Comparison of DSU and MB_s=2 strategies

To demonstrate the NzD strategy in the context of axial SBS dynamic shimming, three strategies (*A, B and C*) were compared. Overall, these approaches vary in terms of how z degeneracy is managed. For "conventional" SBS dynamic shimming [24], *strategy A* uses all available shims (NzD + zD) to shim 19 contiguous 3-slice slabs (57 slices total). The use of three slices in the ROI eliminates the spatial degeneracy in z. *Strategy B* examines the ability of using only the NzD terms to minimize in-plane inhomogeneity and perform SBS shimming with 58 single slice ROIs [16]. Finally, building on the formalism described above, *strategy C* implements multiband shimming MB_s=2 with all NzD+zD terms using only the two targeted slices to form the 29 individual ROIs used for numerical optimization (58 slices total). For MB_s=2, the two single slices forming the ROI were separated by FOV_{slice}/MB_s, 58mm. Notably the MB_s=2 case includes **Z2C2** and **Z2S2** which do not have degenerate partners on the current shim insert. In all three strategies the **Z0** shim was dynamically updated. As a point of reference,

acquisitions were also accompanied by experimentally verified static 1^{st}-2^{nd} and/or static 1^{st}-4^{th+} whole brain shimming.

The B_0 fields were optimized over the brain within the 57 or 58 contiguous 2mm slices spanning the entire brain extending to the mid- or inferior cerebellum. No attempt to center the FOV at isocenter was made. Fig. 2 displays examples of the semi-automatically selected ROIs calculated from gradient echo scout images (2mm thick 128x128 resolution with a FOV of 192x192mm^2). B_0 map data were acquired from the 57 or 58 2-mm contiguous slices using a FOV of 192x192mm^2, matrix size 64x64 and 5 evolution times (ΔTE=1,2,4,8 ms). For static shimming, optimized solutions for 1^{st}-2^{nd} order and 1^{st}-4^{th+} order were calculated and verified by measurement. After 1^{st}-4^{th+} static shimming, a DSU solution was then optimized with the maximum current applied to any single shim (including both static and DSU components) constrained so that their arithmetic sum was between $\pm$5A. Based on the constrained optimization results, the maximum aggregate current used for dynamic updating, switched current, was constrained to be less than 15A (*strategies A* and *C*) or 7.5A (*strategy B*). The shim currents were dynamically updated using empirically determined 2-ms ramps (5 or 10 points per ramp, minimum power supply update time is 200us) immediately prior to each excitation pulse.

Subject distribution

All studies were carried out under IRB approved protocols. For the dynamic shimming evaluation, 3 separate groups of 8 adult subjects were studied. A total of 16 subjects (8 men, 8 women, 23-59 years of age) participated, with 3 subjects participating in all three groups, two in two groups with the remaining 11 subjects participating in a single group. To provide a reference condition, 1^{st}-4^{th+} static shimming was performed in all subjects in all groups. 1^{st}-2^{nd} shimming was also acquired with the initial group evaluating strategy A. No significant differences were measured in the global mean B_0 values for 1^{st}-4^{th+} static shimming between the three groups (24.9$\pm$2.5, 23.7$\pm$3.4 and 23.3$\pm$1.8Hz).

DSU and echo planar imaging

Spin-echo (SE) EPI data were acquired to demonstrate the extent of spatial distortions due to residual B_0 field inhomogeneity with 1^{st}-2^{nd} static, 1^{st}-4^{th+} static and 1^{st}-4^{th+} MB_s=2 DSU shimming. For all acquisitions, multi-slice 2D images were acquired with TR/TE 15s/50ms, FOV 200x200 mm^2, 2mm isotropic over 58 slices with phase encoding in the anterior to posterior direction. An in-plane acceleration factor of 3 with an echo-spacing of 0.9ms was used in combination with MB=2 (matching

the MB_s=2 slices). The relatively long echo spacing was dictated by the strong interaction between the gradient set and the magnet, which results in significant increases in magnet pressure for shorter echo spacings. The long TR was used to minimize SAR concerns. For dynamic updating of the EPI data, the linear shim terms were calculated simultaneously with the higher order spherical harmonic terms and loaded to the Siemens console. MB EPI images were reconstructed offline using a 3D GRAPPA algorithm in kx-ky-kz domain [31] with a reference EPI dataset without multi-band excitation.

Data Analysis and Presentation

For the purpose of qualitative visualization, the B_0 maps acquired for the dynamic updating studies from a single subject's three separate studies (strategies A, B and C) were co-registered (SPM12B, https://www.fil.ion.ucl.ac.uk/spm/) using the scout images from their MB_s=2 study. This yielded 56 complete common slices from the three studies. For quantitative comparisons across the three groups, i.e., slice-wise SDs and measures of whole brain inhomogeneity, the data was analyzed without co-registration to avoid artifacts from inclusion of non-brain pixels at the periphery of the brain.

Results

Constrained optimizations

To minimize the potential for eddy currents and the effects of small imperfections in the characterization of the modeled shim fields, we evaluated the effect of varying the maximum aggregate current constraint on the predicted B_0 inhomogeneity achievable. Although the optimal unconstrained amplitude varied substantially depending upon the location of the slices selected; SMA=14.1+5.1A, SCN=22.6+6.4A, MTL = 42.1+6.6A and CBL=35.6+10.1A, its value across the ten subjects for each ROI is relatively similar (Fig 3). Notably, for maximum aggregate currents of 15A or more, there is very little improvement in the overall B_0 homogeneity across all four slice locations. Thus, a constraint of 15A for aggregate current was used for dynamic updating studies including all shims (strategies A and C) and 7.5A when only the NzD shims (1/2 the number of shims) were used (strategy B).

Dynamic Updating: σB_0^{Brain}

To qualitatively evaluate the performance of the different shim conditions and DSU strategies we co-registered data from a single subject who participated in all three studies. Displayed in Fig. 4A (color scale, +60Hz) and 4B (gray scale, $\pm$10Hz) are B_0 maps acquired with 1^{st}-2^{nd} and 1^{st}-4^{th+} static shims and dynamic updating with 1^{st}-4^{th+} shims using all three DSU strategies for the same subject after co-

registration. For all three shim DSU strategies significant gains across the entire brain are seen when compared with both static 1^{st}-4^{th+} and static 1^{st}-2^{nd} shimming. To quantitatively evaluate the relative performance of the different shim strategies in comparison to static 1^{st}-2^{nd} and 1^{st}-4^{th+} shimming and themselves we calculated the standard deviation for the whole brain, σB_0^{Brain}, for all brain pixels included in the ROIs across all slices without co-registration. Pooling across the 8 subjects σB_0^{Brain} was 32.4±2.6 and 24.9±2.5Hz for 1^{st}-2^{nd} static and 1^{st}-4^{th+} static shimming (Table 2, I and II) respectively. B_0 maps are available in digital format at https://www.rad.pitt.edu/mrrc-shim-data-download.html.

With *strategy A* (conventional SBS shimming using all available shim terms) the achieved σB_0^{Brain} was 15.1±1.7Hz (Table 2, III). In *strategy B*, only the NzD shims were used, thus the maximum aggregate current constraint was reduced to 7.5A, to be consistent with using only one half of the shims. Despite this reduction in aggregate current, the achieved σB_0^{Brain} with DSU strategy B was 14.3±1.5Hz, (Table 2, IV), nearly identical to that achieved with *strategy A*. Although this study was performed in a separate group of subjects, σB_0^{Brain} for static 1^{st}-4^{th+} shimming was also not statistically different, 23.3±1.8 versus 24.9±2.5Hz. For the three subjects who participated in all three DSU strategy groups, their mean σB_0^{Brain} for *strategy B* increased by 2.9±7.3% relative to *strategy A*.

As predicted *strategy C*, MB_s=2 using all available shims (zD and NzD terms), provides nearly equivalent performance to that of SBS-DSU in comparison to strategies A and B (Fig 4). For n=8 subjects, the mean σB_0^{Brain} was 23.7±3.4 and 14.4±2.0Hz for 1^{st}-4^{th+} static and 1^{st}-4^{th+} DSMB_s=2 (Table 2, V) respectively. For the three subjects who participated in all three strategy groups their σB_0^{Brain} for *strategy C* was unchanged relative to *strategy A* (0.0±5.8% change).

Dynamic Updating: σB_0^{Slice}

The aggregate average static 1^{st}-4^{th+} shim current was 8.7±1.5A across all subjects and studies. The maximum absolute current applied for any single shim for any subject was 2.88A for the **Z2** shim. Averaging across all slices and all subjects for *strategies A,B and C* the total aggregate current (sum of static and dynamic), were: 16.6±4.6A (range 7.6-24.5A), 11.3±2.8A (range 5.3-18.4A) and 16.3±3.9A (range 7.5-22.5A) respectively. Notably, the characteristic currents used are similar in *strategies A* and *C* where all shims were used and the maximum aggregate switched current constraint was 15A. As expected, *strategy B* requires less aggregate current consistent with the lower constraint on aggregate switched current (7.5A).

calculated from the experimental B_0 maps. Notably, DSU-MB_S=2 shows improvements in both well shimmed brain regions (Fig 6C) and also in regions prone to large shifts (Fig. 6D).

MB_s>2 dynamic updating

For higher factor MB imaging to achieve the equivalent performance to SBS-DSU, it is necessary to generate NzD B_0 fields at multiple discrete locations simultaneously. In principle this could be achieved with higher degree polynomials as shown in Eqs. 3 (MB_s=3) and 4 (MB_s=4). With increasing MB factor f, it is necessary to have f-1 zD partners for each NzD shim.

$$zD_i(x,y) = c_0 * \mathbf{Z0} + [c_1 z + c_2 z^2] * NzD_i \quad [3]$$

$$zD_i(x,y) = c_0 * \mathbf{Z0} + [c_1 z + c_2 z^2 + c_3 z^3] * NzD_i \quad [4]$$

Although the **Z2X** shim is denoted with a z^2 dependency relative to **X**, the **Z2** family also has an in-plane dependence of (x^2+y^2) and is more accurately considered a NzD shim (this also true for the Z2 shim family including **Z2, Z2Cn, Z2Sn** n=1,2,…). Thus, for MB_s>2, using the NzD shims that mix z and in-plane components will generate less optimal performance in comparison to MB_s=2 or SBS shimming. We evaluated the predicted improvements for DSU when using MB_s=3 and MB_s=4, by simulating the predicted values with the current shim insert for the 8 subjects in group C using an aggregate switched current limit of 15A. Figure 7 shows calculations for a single individual (same as shown in Figs 4-6) using 1^{st}-4^{th+} static shimming, and MB_s=1,2,3 and 4 on a slice-by-slice basis. As expected, MB_s=1 (SBS) with the NzD shims and MB_s=2 using all available shims are nearly identical. However, while MB_s=3 and MB_s=4 show some progressive loss in achieved homogeneity, it is notable that MB_s=4 still achieves superior global homogeneity, σB_0^{Brain} than static 1^{st}-4^{th+} shimming (Table 2, VI and VII). Since the homogeneity for MB_s=2 to 4 is optimized in 2-4 slice blocks, the improvement in homogeneity is over all pixels within the block, thus individual slices within the block may show a higher SD than their 1^{st}-4^{th} order static equivalent for shimming.

Discussion

Strategies for dynamic shimming

In this work we have demonstrated that implementation of a very high order spherical harmonic shim insert coil with dynamic shim updating gives significant improvements over static shimming. This was achieved with relatively minor pre-emphasis corrections (limited to **Z0** and the shims on the gradient

As described, σB_0^{Brain} is very similar for the three different shim strategies (A,B and C). To evaluate the performance on a slice-by-slice basis, Fig. 5 displays the achieved slice-wise standard deviation (σB_0^{Slice}) as a function of slice position (slice #1 is the most inferior slice) for the same subject presented in Fig. 4. To avoid potential errors in this quantitative data associated with imperfections in co-registration (i.e. inclusion of non-brain regions at the periphery), the data is presented as acquired without co-registration. The data is grouped according to shim type (static 1^{st}&2^{nd}, static 1^{st}-4^{th+} and DSU 1^{st}-4^{th+}) and averaged over the three study sessions (DSU strategies A, B and C) with "error bars" indicating the standard deviations within a group across study sessions. Consistent with Fig. 4, the largest improvements in homogeneity for static 1^{st}-4^{th+} shimming over static 1^{st}&2^{nd} shimming are found in the cerebellum and temporal lobe (slices 1-3) and superior brain regions (slices 40-55). The largest improvements in homogeneity for DSU over static 1^{st}-4^{th+} shims is seen in dynamic updating using 3 slice ROIs the cerebellum and inferior temporal lobe (slices 1-15) and inferior frontal lobe (slices 22-28). Improvements over the superior brain slices (29-55) are significant but more modest, i.e. <5Hz. Notably, across much of the superior half of the brain σB_0^{Slice} < 10Hz for all three DSU shim strategies. Pooling the 8 subjects in each DSU shim group, 27.0±2.7, 26.3±5.2 and 27.8±7.1 of the slices achieved σB_0^{Slice} of <10Hz, enabling the intrinsic 4-5Hz difference in gray and white matter susceptibility at 7T [32, 33] to be visualized Figure 4B.

The variability in Fig.5 has both positional variability (head position and rotation) and potential differences arising from the different shim strategies used. The largest "error bars" are found in slices 7 and 8 (inferior edge of the temporal lobe) and 16-22 (inferior edge of the anterior frontal lobe) where the spatial gradients in susceptibility are the largest in the z direction. Despite the positional differences between the three studies, the "error bars" are relatively small indicating good agreement between the different strategies on a slice by slice basis.

Spin echo EPI with MB_s=2

Fig. 6 shows selected regions of the frontal (A) and temporal (B) lobes from whole brain spin echo EPI data acquired with static 1^{st}-2^{nd}, static 1^{st}-4^{th+}, and with dynamic 1^{st}-4^{th+} (MB_s=2 DSU) shimming (strategy C) from the same subject shown in Figs 4 and 5. All images are available for evaluation in Supporting Information Figure S1. The MB_s=2 DSU images retain greater fidelity to the brain contours in comparison to 1^{st}&2^{nd} order static shimming in both the frontal and temporal slices and in comparison to static 1^{st}-4^{th} order static shimming in the temporal slices. Figure Figs 6C and D show the distribution of pixels shifts (34.7Hz/pixel) for static 1^{st}-2^{nd}, static 1^{st}-4^{th+}, and with dynamic 1^{st}-4^{th+} (MB_s=2 DSU)

set, i.e. 2nd orders), use of 2ms ramps for all shim changes and constraining the maximum aggregate switched current to 7.5 or 15A after static 1st-4th+ shimming. Thus, the maximal shim offsets for any given shim channel of any slice during dynamic shimming reflects both the dynamic and static components. These values will vary depending upon whether or not static shimming is performed first. If any static offset adds destructively to its corresponding dynamic component and the dynamic components reach the maximum aggregate dynamically switched constraint, then the values (static + dynamic) used with or without static shimming may differ. Limiting the aggregate switched current minimizes potential eddy current effects and inaccuracies in high amplifier outputs and shim field modeling. Previously, Schwerter [20] reported that eddy current effects could be minimized by using ramped changes and limiting the change in current to 0.5A between consecutive shim updates. While Schwerter's approach is more direct in minimizing dB_0/dt directly, the needed transition from the slices at the extremes of the brain (during SBS shimming) requires additional algorithmic complexity. In the present work, the use of an aggregate current constraint is sufficient to achieve improvements of 53 and 39% relative to static shimming with 1st-2nd and 1st-4th+ shims. Notably all three dynamic shim strategies achieved similar fractional improvements (39.4, 38.7 and 39.2% respectively) in B_0 homogeneity in comparison to their 1st-4th+ static shimming equivalent.

Multi-band shimming

The partitioning of the spherical harmonic terms with respect to their spatial dependence in the z direction shows that the in-plane shim performance over thin axial slices is largely governed theoretically and experimentally by the NzD shims. As a result, omission of the zD, z-degenerate shims, has relatively little impact on the achieved results for slice-by-slice shimming. To this end, the requirement of shimming over multi-slice slabs to constrain values in the zD terms is not necessary when the zD shims are omitted, simplifying the shimming process from both a software and hardware perspective. More importantly however is that the zD shim terms can be used to support MB_s=2 imaging with in-plane homogeneity equivalent to full SBS shimming. When each NzD shim has a zD partner available with sufficient efficiency and strength, for thin axial slices, MB_s=2 shimming provides near equivalent performance as SBS shimming. As expected, spin echo echo-planar images acquired with MB_s=2 DSU shows greater spatial fidelity of the images, consistent with a reduction in pixel overlap and spatial distortion.

For higher MB factor shimming, the spatial dependence of the SHs deviate from that needed to replicate the NzD shims at more than two z slice locations simultaneously. Despite this effect, MB_s=3 and MB_s=4 shimming is predicted to provide significant improvements, 25% and 15%, over that of static 1^{st}-4^{th+} shimming and 43% and 35% over 1^{st}-2^{nd} static shimming respectively. Theoretically, equivalent performance for SBS for arbitrary MB_s factor f, can be maintained as long as the hardware is capable of simultaneously generating shim fields of the non-degenerate SHs with the desired scalings at f positions along the z axis. As exemplified in Eq. 4 for f=4, this condition is of interest for shim coil design for optimal dynamic slice updating.

Limitations

The performance of multi-band shimming of thin axial slices is predicated on the strength of the zD shims to generate the needed NzD equivalent spatial distributions at disparate z locations. Our experimental data indicates that for the shim insert used, this is a valid assumption for the MB_s=2 case. Based on targeting of sufficiently thin axial slices over which there is minimal generated B_0 field in the z direction, the theory underlying this approach focuses this initial work on pure axial slices. The use of a 2mm slice thickness is thicker than that recommended for DTI and fMRI at 3T, 1.5mm and 2mm and 7T 1.05mm and 1.6mm respectively (https://protocols.humanconnectome.org/HCP/3T/imaging-protocols.html, https://protocols.humanconnectome.org/HCP/7T/). The extent to which the experimental performance can be maintained when the slices are angulated is beyond the scope of this work. Nonetheless, strategy C is highly effective and should be highly relevant for DTI where pure axial images and spin echo acquisitions are common. For gradient echo EPI acquisitions, through plane losses will be dependent on the slice thickness, pulse sequence and parameters used and residual $\partial B_0/\partial z$. However, DSU strategy A implicitly controls through plane losses by optimizing over a three slice slab. For DSU strategy B, when the DSU corrections are applied after whole brain shimming (which would tend to reduce through plane losses) the applied corrections are almost entirely in-plane, except for **Z2Cn** and **Z2Sn** family of shims. In this case the much greater extent of the ROI for each slice in the in-plane direction and high pure in-plane dependencies (x^n and y^n : n=2,3,4, Table 1) typically constrains the maximal value of the shims, limiting their effect on $\partial B_0/\partial z$. For DSU strategy C where the intrinsic z dependence of the zD shims is used to generate different NzD fields at different locations along z, it is important that the slice thickness used is sufficiently thin so as to limit through plane losses, i.e. slice thickness*$\partial B_0/\partial z$.

Comparative performance

Comparisons of different hardware configurations for shimming can be challenging due to a variety of factors including: 1) subject demographics, 2) differences in sampling coverage and ROI definition, including extracerebral components and voxel exclusion criteria, 3) base magnet performance and any perturbations to the B_0 homogeneity associated with in-bore hardware differences, 4) accuracy of the modeling of the fields generated by the shims and 5) accuracy of the acquired and reconstructed B_0 maps, e.g. resolution, maximum duration of B_0 encoding, SNR and other protocol details. While all of these factors can influence shimming performance, accurate field mapping is critical. Use of small pixels (i.e. lower SNR) and short maximal B_0 evolution times (reduced phase/Hz dynamic range) will reduce accuracy [34] , while longer minimum B_0 evolution times place greater reliance on unwrapping routines [35] and very large pixels in extremely inhomogeneous regions can be lost due to intravoxel dephasing. Table 3 provides comparisons with recent literature reports. The present data are consistent with our previous report [6] using static shimming, with an 11% increase in inhomogeneity associated with the increase in slice coverage from 99 to 114-116mm. As an independent and endogenous measure of homogeneity, the ability to visualize the intrinsic gray/white matter susceptibility difference across a large fraction of the brain provides a "ground-truth" assessment and argues for both the accuracy of the mapping and performance of the methods and hardware. Use of the VHOS insert (which includes nearly all 4^{th} order terms) results in the visually evident remaining inhomogeneities being largely dominated by intrinsic gray/white matter differences or C5/S5 contributions, suggesting that in-plane inhomogeneities up through 4^{th} order have been largely eliminated. For all 3 DSU methods, over the superior 4cm of the brain, σB_0 on a slice-by-slice basis approaches 4-5Hz. At this level of performance, the remaining inhomogeneity is largely dominated by the intrinsic susceptibility difference between gray and white matter.

Conclusions

DSU with a very high degree spherical harmonic shim insert reduces the B_0 inhomogeneity in the human brain at 7T, from a mean of 24.9±2.5Hz (static 1^{st}-4^{th+}) to 15.1±1.7Hz (SBS-DSU). Analysis of the spatial dependence of the spherical harmonic terms shows that MB_s with equivalent performance to SBS shimming is theoretically possible. With the current spherical harmonic shim insert, this was experimentally verified with MB_s=2, giving 14.4±2.0Hz inhomogeneity and a reduction in in-plane distortions in EPI data.

Table 1: Spatial dependence, degeneracy and strength of spherical harmonic shims

NzD:	Spatial dependence	Strength Hz/mm^n at 5A	zD:	Spatial dependence	Strength Hz/mm^n at 5A
Z0	C_0		Z	z	
X	x		ZX	zx	-5.92E-02
Y	y		ZY	zy	-5.84E-02
Z2	$z^2-(x^2+y^2)/2$	-7.34E-02	Z3	$z(z^2-3(x^2+y^2)/2)$	2.55E-03
C2	x^2-y^2	-2.78E-02	ZC2	$z(x^2-y^2)$	6.23E-03
S2	2xy	-2.84E-02	ZS2	z(2xy)	-6.14E-03
Z2X	$x(z^2-((x^2+y^2)/4))$	-9.04E-03	Z3X	$z(x(z^2-(3(x^2+y^2)/4)))$	-6.47E-05
Z2Y	$y(z^2-((x^2+y^2)/4))$	-8.86E-03	Z3Y	$z(y(z^2-(3(x^2+y^2)/4)))$	6.15E-05
C3	$x(x^2-3y^2)$	-9.65E-04	ZC3	$z(x(x^2-3y^2))$	6.36E-05
S3	$y(3x^2-y^2)$	9.51E-04	ZS3	$z(y(3x^2-y^2))$	-6.17E-05
Z4 – NA	$z^4-3z^2(x^2+y^2)+3((x^2+y^2)^2)/8$		Z5 - NA	$z(z^4-5z^2(x^2+y^2)+15((x^2+y^2)^2)/8$	
Z2C2	$(x^2-y^2)(z^2-((x^2+y^2)/6))$	4.74E-05	Z3C2 - NA	$z(x^2-y^2)(z^2-((x^2+y^2)/2))$	
Z2S2	$(2xy)(z^2-((x^2+y^2)/6))$	-4.52E-05	Z3S2 - NA	$z(2xy)(z^2-((x^2+y^2)/2))$	
C4	$x^4-6x^2y^2+y^4$	9.46E-06	ZC4	$z(x^4-6x^2y^2+y^4)$	3.00E-07
S4	$4xy(x^2-y^2)$	-9.70E-06	ZS4	$z(4xy(x^2-y^2))$	-2.90E-07

NzD – non z-degenerate shim, zD – z-degenerate shim, NA – not available on the shim insert.

Table 2: Group results for different shimming methods

Table 1	Method	Shims Used	MB_s	Data	N	SD (Hz)
I	Static	1^{st}-2^{nd}	1	MSD	8	32.4±2.6
II	Static	1^{st}-4^{th+}	1	MSD	8	24.9±2.5
III	Dynamic (A)	1^{st}-4^{th+}	1	MSD	8	15.1±1.7
IV	Dynamic (B)	NzD	1	MSD	8	14.3±1.5
V	Dynamic (C)	1^{st}-4^{th+}	2	MSD	8	14.4±2.0
VI	Dynamic	1^{st}-4^{th+}	3	PRED	8	18.6±3.2
VII	Dynamic	1^{st}-4^{th+}	4	PRED	8	21.2±3.4

MSD - measured, PRED – predicted, (A,B,C) – DSU strategy

Table 3: Comparison with previously reported data

	This report	Ref. [24]	Ref. [9]
Configuration	SH 1^{st}-4^{th+}	32 Ch. MC	48 Ch. MC
Slice Coverage	114-116mm	124mm	117mm
Resolution	3x3x2mm^3	2.4x2.4x2mm^3	1.7x3.4x3mm^3
ΔTE Times	1,2,4 and 8ms	1.02ms	0.33,1 and 3ms‡
Static	24.9±2.5	41.2±6.2*	
MB=1	15.1±1.7 (39%) **(A)**	23.7±5.0* (43%)	13.3±1.7
MB=1	14.3±1.5 (43%) **(B)**		
MB=2	14.4±2.0 (42%) **(C)**	27.6±5.6* (33%)	
MB=3	18.6±3.2* (25%)	33.3±5.7* (19%)	
MB=4	21.2±3.4* (15%)		

SH - spherical harmonic, MC - multi-coil, ‡ Parameters used for initial field map, *Simulated value, **(A,B,C)** – DSU strategy used, % reflects the % improvement relative to static shimming

Comparative performance

Comparisons of different hardware configurations for shimming can be challenging due to a variety of factors including: 1) subject demographics, 2) differences in sampling coverage and ROI definition, including extracerebral components and voxel exclusion criteria, 3) base magnet performance and any perturbations to the B_0 homogeneity associated with in-bore hardware differences, 4) accuracy of the modeling of the fields generated by the shims and 5) accuracy of the acquired and reconstructed B_0 maps, e.g. resolution, maximum duration of B_0 encoding, SNR and other protocol details. While all of these factors can influence shimming performance, accurate field mapping is critical. Use of small pixels (i.e. lower SNR) and short maximal B_0 evolution times (reduced phase/Hz dynamic range) will reduce accuracy [34] , while longer minimum B_0 evolution times place greater reliance on unwrapping routines [35] and very large pixels in extremely inhomogeneous regions can be lost due to intravoxel dephasing. Table 3 provides comparisons with recent literature reports. The present data are consistent with our previous report [6] using static shimming, with an 11% increase in inhomogeneity associated with the increase in slice coverage from 99 to 114-116mm. As an independent and endogenous measure of homogeneity, the ability to visualize the intrinsic gray/white matter susceptibility difference across a large fraction of the brain provides a "ground-truth" assessment and argues for both the accuracy of the mapping and performance of the methods and hardware. Use of the VHOS insert (which includes nearly all 4^{th} order terms) results in the visually evident remaining inhomogeneities being largely dominated by intrinsic gray/white matter differences or C5/S5 contributions, suggesting that in-plane inhomogeneities up through 4^{th} order have been largely eliminated. For all 3 DSU methods, over the superior 4cm of the brain, σB_0 on a slice-by-slice basis approaches 4-5Hz. At this level of performance, the remaining inhomogeneity is largely dominated by the intrinsic susceptibility difference between gray and white matter.

Conclusions

DSU with a very high degree spherical harmonic shim insert reduces the B_0 inhomogeneity in the human brain at 7T, from a mean of 24.9±2.5Hz (static 1^{st}-4^{th+}) to 15.1±1.7Hz (SBS-DSU). Analysis of the spatial dependence of the spherical harmonic terms shows that MB_s with equivalent performance to SBS shimming is theoretically possible. With the current spherical harmonic shim insert, this was experimentally verified with MB_s=2, giving 14.4±2.0Hz inhomogeneity and a reduction in in-plane distortions in EPI data.

standard deviation across the three imaging sessions including the three different DSU strategies. Co-registration was not performed.

Figure 6

Figure 6 displays data from the same individual as in Figs 4 and 5. Spin echo echo planar images from frontal (A) and temporal (B) regions, acquired with static 1^{st}-2^{nd}, static 1^{st}-4^{th+} and MB_s=2 DSU 1^{st}-4^{th+}shimming. All images were acquired with GRAPPA=3, an echo spacing of 0.9ms and a multi-band imaging factor (MB_i) of 2. Panel C displays data quantifying the extent of pixel shift for static 1^{st}-2^{nd} (red), static 1^{st}-4^{th+} (blue) and MB_s=2 DSU 1^{st}-4^{th+} (green) shimming for the entire brain based on the acquired B_0 maps. To better visualize the extent to which pixels with large shifts (>5 pixel shift) are present Fig 6D displays pixel shifts in the ranges of -10 to +10 at a different scale.

Figure 7

Figure 7 displays a plot of the SD of the predicted B_0 inhomogeneity on a slice-by-slice basis for static 1^{st}-4^{th}+ degree shimming (measured), MB=1 with NzD shims (simulated); MB=2 (measured), 3 (simulated) and 4 (simulated) with all shims i.e. NzD + zD shims.

References

1. Farzaneh, F., S.J. Riederer, and N.J. Pelc, *Analysis of T2 limitations and off-resonance effects on spatial resolution and artifacts in echo-planar imaging.* Magn Reson Med, 1990. **14**(1): p. 123-39.
2. Jezzard, P. and S. Clare, *Sources of distortion in functional MRI data.* Hum Brain Mapp, 1999. **8**(2-3): p. 80-5.
3. Zhao, Y., A.W. Anderson, and J.C. Gore, *Computer simulation studies of the effects of dynamic shimming on susceptibility artifacts in EPI at high field.* J Magn Reson, 2005. **173**(1): p. 10-22.
4. Wilson, J.L., M. Jenkinson, and P. Jezzard, *Optimization of static field homogeneity in human brain using diamagnetic passive shims.* Magn Reson Med, 2002. **48**(5): p. 906-14.
5. Koch, K.M., et al., *Sample-specific diamagnetic and paramagnetic passive shimming.* J Magn Reson, 2006. **182**(1): p. 66-74.
6. Kim, T., et al., *Gradient-echo EPI using a high-degree shim insert coil at 7T: Implications for BOLD fMRI.* Magnetic resonance in medicine, 2016.
7. Pan, J.W., K.-M. Lo, and H.P. Hetherington, *Role of very high order and degree B0 shimming for spectroscopic imaging of the human brain at 7 tesla.* Magnetic resonance in medicine, 2012. **68**(4): p. 1007-17.
8. Hetherington, H.P., et al., *Robust fully automated shimming of the human brain for high-field 1H spectroscopic imaging.* Magnetic resonance in medicine, 2006. **56**(1): p. 26-33.
9. Juchem, C., et al., *Dynamic multi-coil shimming of the human brain at 7 T.* J Magn Reson, 2011. **212**(2): p. 280-8.
10. Stockmann, J.P., et al., *A 32-channel combined RF and B shim array for 3T brain imaging.* Magn Reson Med, 2015.
11. Han, H., A.W. Song, and T.K. Truong, *Integrated parallel reception, excitation, and shimming (iPRES).* Magn Reson Med, 2013. **70**(1): p. 241-7.
12. Zhou, J., et al., *An orthogonal shim coil for 3T brain imaging.* Magn Reson Med, 2020. **83**(4): p. 1499-1511.
13. Jia, F., et al., *Design of a shim coil array matched to the human brain anatomy.* Magn Reson Med, 2020. **83**(4): p. 1442-1457.
14. Blamire, A.M., D.L. Rothman, and T. Nixon, *Dynamic shim updating: a new approach towards optimized whole brain shimming.* Magn Reson Med, 1996. **36**(1): p. 159-65.
15. de Graaf, R.A., et al., *Dynamic shim updating (DSU) for multislice signal acquisition.* Magn Reson Med, 2003. **49**(3): p. 409-16.
16. Koch, K.M., et al., *Dynamic shim updating on the human brain.* J Magn Reson, 2006. **180**(2): p. 286-96.
17. Sengupta, S., et al., *Dynamic B0 shimming at 7 T.* Magn Reson Imaging, 2011. **29**(4): p. 483-96.
18. Juchem, C., et al., *Dynamic Shimming of the Human Brain at 7 Tesla.* Concepts Magn Reson Part B Magn Reson Eng, 2010. **37B**(3): p. 116-128.
19. Sengupta, S., et al., *Software compensation of eddy current fields in multislice high order dynamic shimming.* J Magn Reson, 2011. **210**(2): p. 218-27.
20. Schwerter, M., et al., *Interslice current change constrained B0 shim optimization for accurate high-order dynamic shim updating with strongly reduced eddy currents.* Magn Reson Med, 2019. **82**(1): p. 263-275.
21. Fillmer, A., et al., *Fast iterative pre-emphasis calibration method enabling third-order dynamic shim updated fMRI.* Magn Reson Med, 2016. **75**(3): p. 1119-31.
22. Vannesjo, S.J., et al., *Gradient and shim pre-emphasis by inversion of a linear time-invariant system model.* Magn Reson Med, 2017. **78**(4): p. 1607-1622.

23. Hetherington H, M.C., Pan J, *Dynamically updated B0 shimming for multi-band imagiong with high iorder spherical harmonics*, in *International Society of Magnetic Resonance in Medicine*. 2019: Montreal Canada.
24. Stockmann, J.P. and L.L. Wald, *In vivo B0 field shimming methods for MRI at 7T.* Neuroimage, 2018. **168**: p. 71-87.
25. Liao, C., et al., *High-fidelity, high-isotropic-resolution diffusion imaging through gSlider acquisition with B 1 + and T1 corrections and integrated DeltaB0 /Rx shim array.* Magn Reson Med, 2020. **83**(1): p. 56-67.
26. Shen, J., et al., *Linear projection method for automatic slice shimming.* Magn Reson Med, 1999. **42**(6): p. 1082-8.
27. Avdievich, N.I., *Transceiver-Phased Arrays for Human Brain Studies at 7 T.* Appl Magn Reson, 2011. **41**(2-4): p. 483-506.
28. Avdievich, N.I., et al., *Short echo spectroscopic imaging of the human brain at 7T using transceiver arrays.* Magn Reson Med, 2009. **62**(1): p. 17-25.
29. Hetherington, H.P., et al., *RF shimming for spectroscopic localization in the human brain at 7 T.* Magn Reson Med, 2010. **63**(1): p. 9-19.
30. Hetherington, H.P., et al., *Robust fully automated shimming of the human brain for high-field 1H spectroscopic imaging.* Magn Reson Med, 2006. **56**(1): p. 26-33.
31. Moon CH, H.H., Pan JW, *Full 3D ky-kz-kx GRAPPA reconstruiction of SMS MB EPI*, in *International Society of Magnetic Resonance in Medicine*. 2019: Montreal Canada.
32. Marques, J.P., et al., *On the origin of the MR image phase contrast: an in vivo MR microscopy study of the rat brain at 14.1 T.* Neuroimage, 2009. **46**(2): p. 345-52.
33. He, X. and D.A. Yablonskiy, *Biophysical mechanisms of phase contrast in gradient echo MRI.* Proc Natl Acad Sci U S A, 2009. **106**(32): p. 13558-63.
34. Gruetter, R., *Automatic, localized in vivo adjustment of all first- and second-order shim coils.* Magn Reson Med, 1993. **29**(6): p. 804-11.
35. Jenkinson, M., *Fast, automated, N-dimensional phase-unwrapping algorithm.* Magn Reson Med, 2003. **49**(1): p. 193-7.

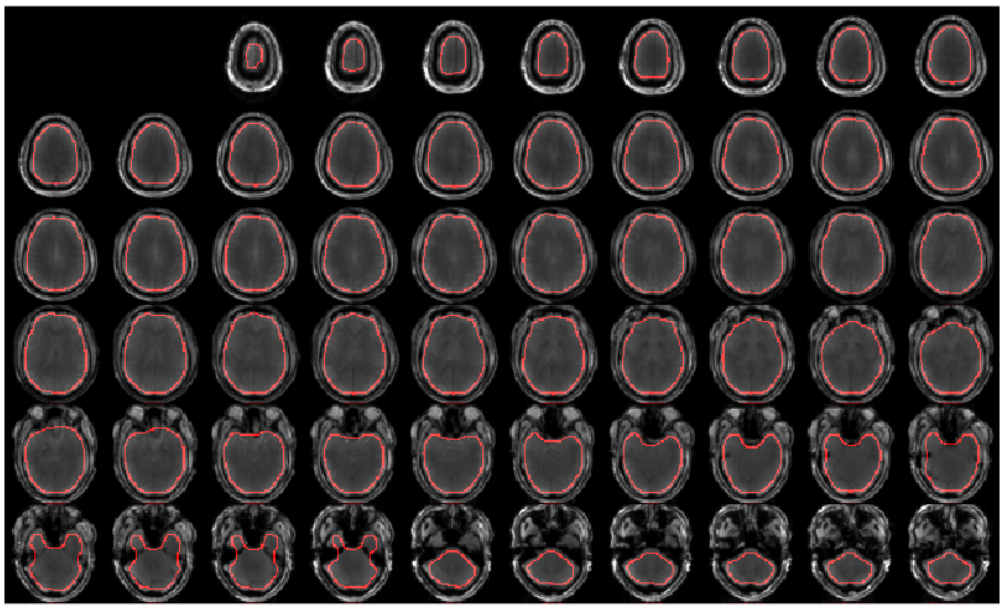

Figure 2 displays the boundary for the ROIs for optimization and analysis are shown in red.

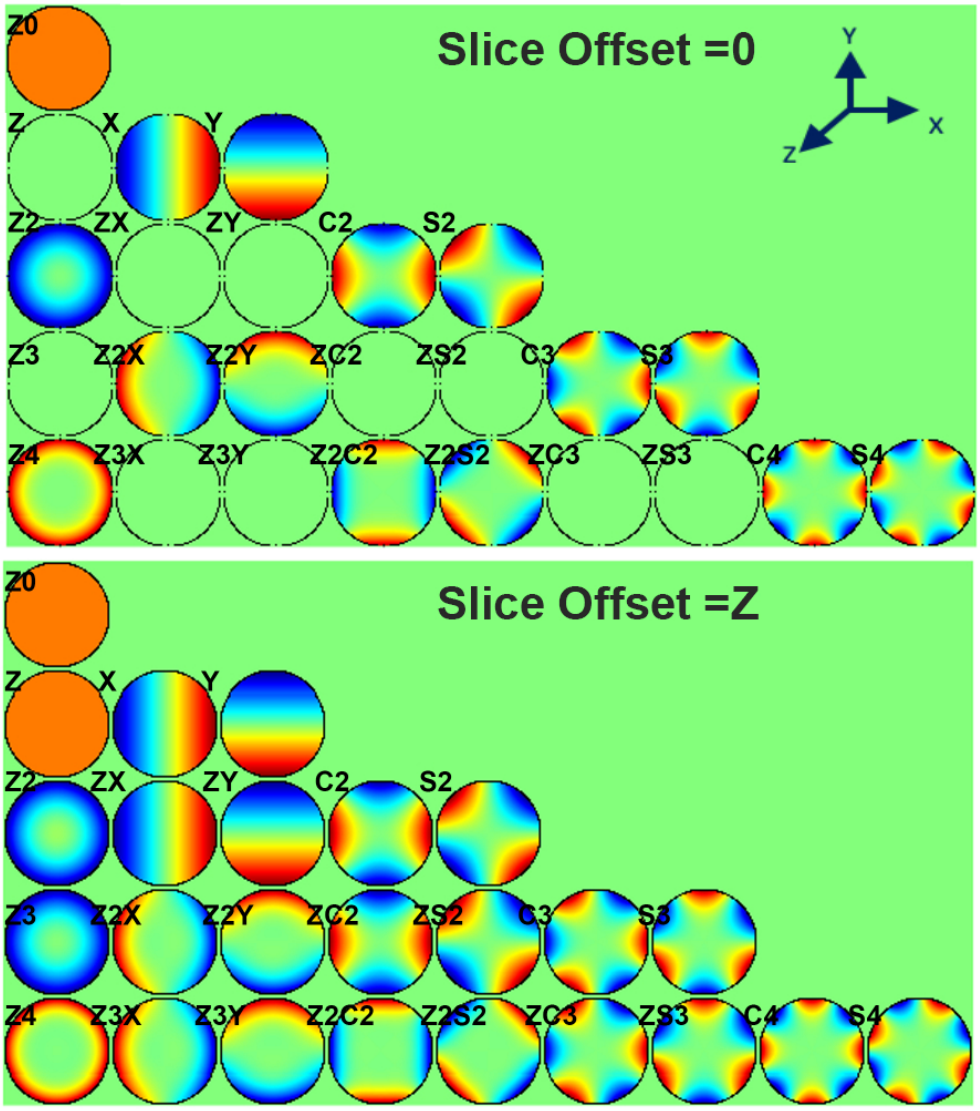

Figure 1 displays theoretical axial plots of the shims demonstrating the concept of degeneracy in the z direction. The plots are calculated at iso-center and at an unspecified offset in the z direction and scaled to maximize the color scale. Degenerate pairs of shims can be identified in the lower plot (Slice Offset =Z) by shims with equivalent spatial dependencies in adjacent rows. The zD shims are those with no amplitude in the Slice Offset=0 group.

76x86mm (300 x 300 DPI)

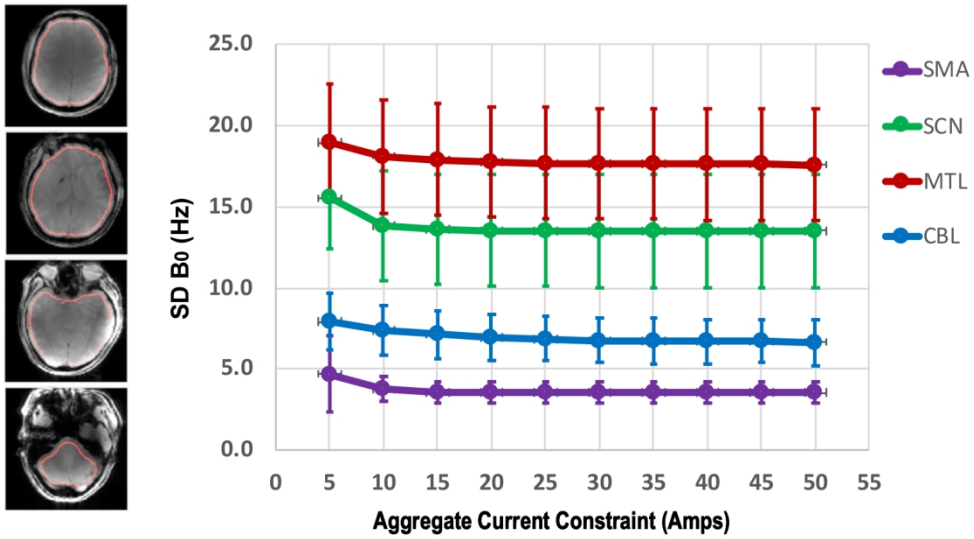

Figure 3 displays plots of the SD of the inhomogeneity over 4 representative brain ROIs as a function of a constraint on the maximal aggregate current averaged over 10 subjects. The data is from 4 representative ROIs (far left) with slices including: SMA - secondary motor area; SCN – subcortical nuclei; TL – temporal lobe; and CBL – cerebellum.

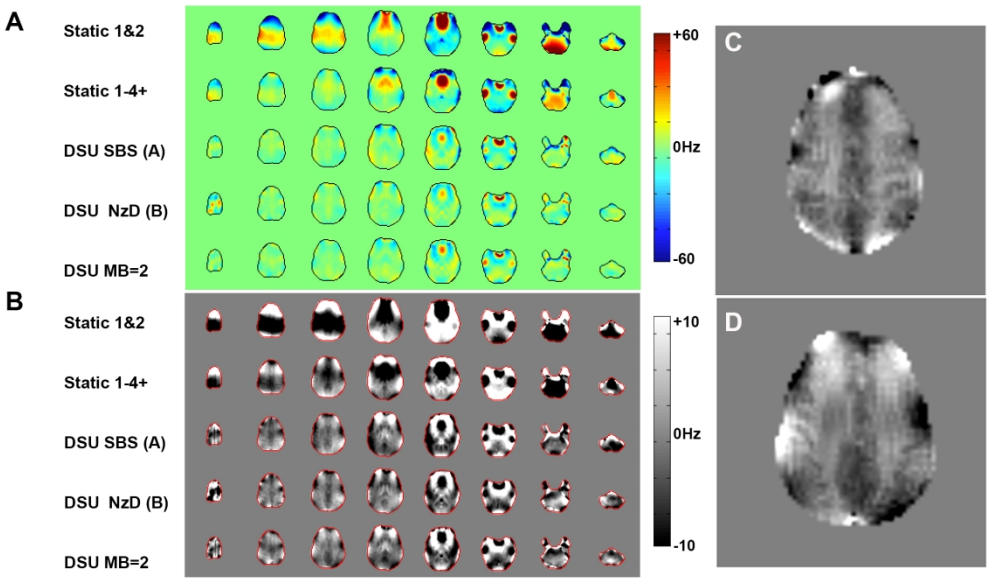

Figures 4A and 4B display B_0 maps from a single individual for 1^{st}-2^{nd} degree static shimming, 1^{st}-4^{th+} static shimming and 1^{st}-4^{th+} DSU shimming with strategies A, B and C. The maps are presented on a color scale of +60Hz and +10Hz and the target ROI is outlined in black and red respectively. The data was co-registered and every 8th slice and the most superior slice are displayed. Figures 4C and 4D show two representative slices from superior brain regions in gray scale for strategy C, DSU MB_s=2.

190x113mm (300 x 300 DPI)

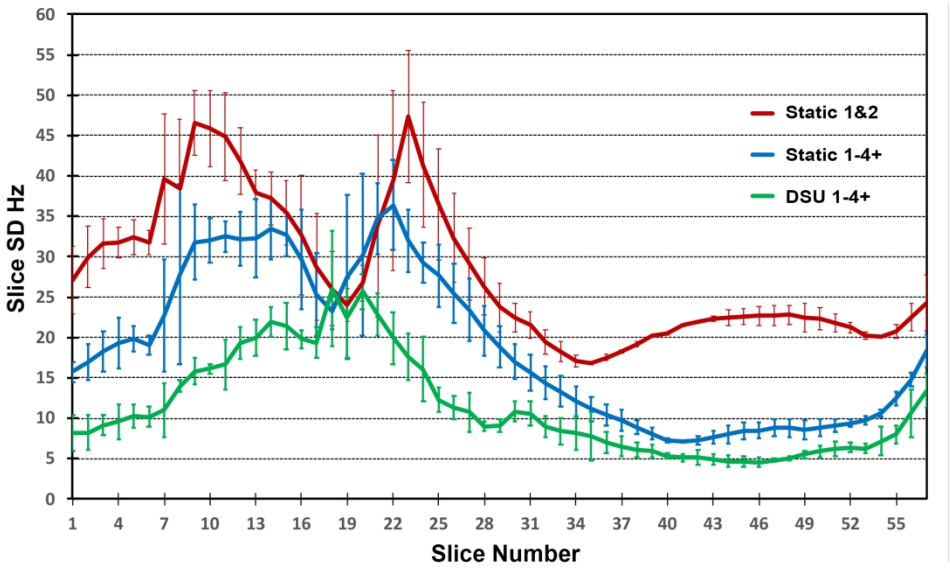

Figure 5 displays data from the same individual as in Fig 4. showing the standard deviation per slice on a slice-wise basis (slice #1 is the most inferior slice) for the different shim conditions, 1^{st}-2^{nd} degree static shimming (red), 1^{st}-4^{th+} static shimming (blue) and 1^{st}-4^{th+} DSU shimming with strategies A, B and C (green) averaged over the three different imaging sessions. The "error bars" reflect the calculated standard deviation across the three imaging sessions including the three different DSU strategies. Co-registration was not performed.

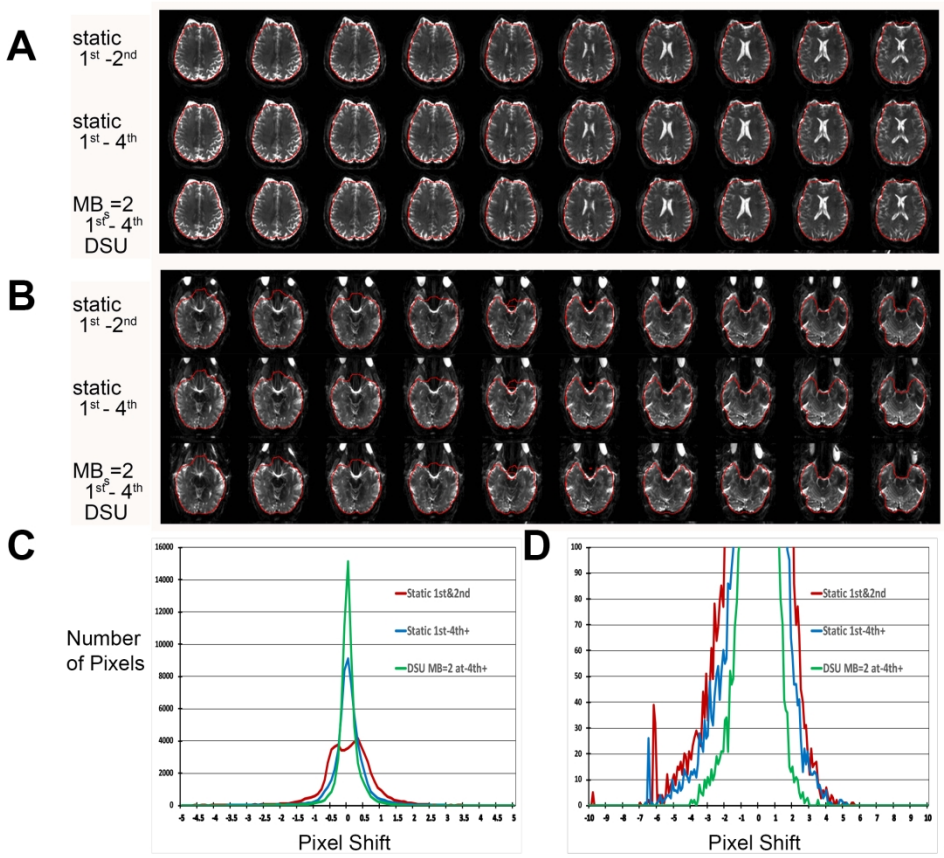

Figure 6 displays data from the same individual as in Figs 4 and 5. Spin echo echo planar images from frontal (A) and temporal (B) regions, acquired with static 1st-2nd, static 1st-4th+ and MBs=2 DSU 1st-4th+shimming. All images were acquired with GRAPPA=3, an echo spacing of 0.9ms and a multi-band imaging factor (MBi) of 2. Panel C displays data quantifying the extent of pixel shift for static 1st-2nd (red), static 1st-4th+ (blue) and MBs=2 DSU 1st-4th+ (green) shimming for the entire brain based on the acquired B0 maps. To better visualize the extent to which pixels with large shifts (>5 pixel shift) are present Fig 6D displays pixel shifts in the ranges of -10 to +10 at a different scale.

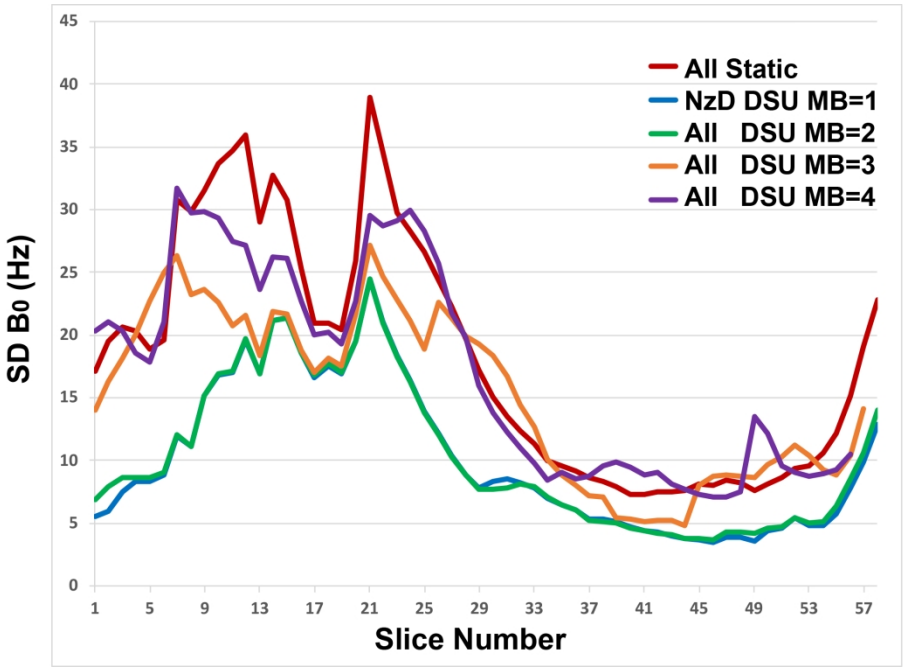

Figure 7 displays a plot of the SD of the predicted B_0 inhomogeneity on a slice-by-slice basis for static 1^{st}-4^{th+} degree shimming (measured), MB_s=1 with NzD shims (simulated); MB_s=2 (measured), 3 (simulated) and 4 (simulated) with all shims i.e. NzD + zD shims.